Scientific Research Publishing

Advances in Nanoparticles, 2025, 14(4), 121-141
https://www.scirp.org/journal/anp
ISSN Online: 2169-0529
ISSN Print: 2169-0510

Synthesis and Characterization of Eco-Friendly Fe_3O_4/g-C_3N_4/rGO Nanocomposites for Photodegradation of Methylene Blue Dye

Sanju Mahich[1,2], Kundan Singh Shekhawat[3], Shubham Gupta[1], Anuj Kumar[4], Sanjay Kumar Swami[5], Jaya Mathur[3], Vijay Devra[2], Amanpal Singh[1]

[1]Department of Physics, University of Rajasthan, Jaipur, Rajasthan, India
[2]Janki Devi Bajaj Government Girls College, Kota, Rajasthan, India
[3]Department of Chemistry, University of Rajasthan, Jaipur, Rajasthan, India
[4]Department of Physics, J.C. Bose University of Science and Technology, YMCA, Faridabad, Haryana, India
[5]School of Advanced Materials, Green Energy and Sensor Systems, Indian Institute of Engineering Science and Technology, Shibpur, Botanic Garden, Howrah, West Bengal, India
Email: amanbkn@gmail.com

How to cite this paper: Mahich, S., Shekhawat, K.S., Gupta, S., Kumar, A., Swami, S.K., Mathur, J., Devra, V., Singh, A. (2025) Synthesis and Characterization of Eco-Friendly Fe_3O_4/g-C_3N_4/rGO Nanocomposites for Photodegradation of Methylene Blue Dye. *Advances in Nanoparticles*, **14**, 121-141.
https://doi.org/10.4236/anp.2025.144008

Received: September 1, 2025
Accepted: October 24, 2025
Published: October 27, 2025

Abstract

Fe_3O_4/g-C_3N_4/rGO nanocomposites were synthesized as visible light-powered, eco-friendly photocatalysts for treating dye-polluted wastewater. Methylene blue (MB) served as the model contaminant. The composite aimed to improve charge separation and light harvesting by integrating g-C_3N_4 with conductive rGO and catalytically active Fe_3O_4. X-ray diffraction (XRD), Fourier-transform infrared spectroscopy (FTIR), field-emission scanning electron microscopy (FESEM), and energy-dispersive X-ray spectroscopy (EDX) were employed to analyze the microstructure, morphology, and elemental composition, as well as to assess compositional uniformity. Brunauer-Emmett-Teller (BET) and Barrett-Joyner-Halenda (BJH) analysis confirmed the mesoporous nature of the Fe_3O_4/g-C_3N_4/rGO composite, with a specific surface area of 25.55 m^2/g, a pore volume of 0.0236 cc/g, and an average pore diameter of 3.37 nm. UV-Vis diffuse reflectance spectroscopy (UV-Vis DRS) revealed that the nanocomposites possess enhanced absorption in the visible-light region, characterized by a distinct absorption edge around 475 nm. Photocatalytic tests under visible light irradiation demonstrated a remarkable degradation efficiency of 99.53% for MB dye at pH 11, significantly outperforming the individual components. Liquid Chromatography-Mass Spectrometry (LC-MS) confirmed the presence of in-

termediate products, supporting a stepwise degradation mechanism of MB through demethylation and oxidative reactions.

Keywords

Environmental Remediation, Methylene Blue, Mesoporous, Fe_3O_4/g-C_3N_4/rGO Nanocomposite

1. Introduction

Clean water is essential for all living organisms, yet its quality is increasingly affected by pollution from industrialization and rising living standards. Toxic synthetic pollutants from industrial and domestic wastewater significantly disrupt ecosystems and pose serious risks to human health, making pollution control a critical global challenge. Each day, approximately 2 million tons of waste are discharged into water systems, with 17% - 20% of industrial wastewater attributed to synthetic dyes, according to World health organization statistics [1] [2]. Industries such as textiles, printing, and tanneries are major sources of dye wastewater pollution. Synthetic dyes, including MB, are particularly hazardous due to their toxicity and potential carcinogenicity, highlighting the urgent need for their removal from industrial effluents [3]. The development and implementation of effective wastewater treatment technologies are therefore essential to eliminate these persistent, non-biodegradable dyes and enable safe reuse of treated water.

Various chemical, physical, and biological treatment methods have been developed for pollutant removal. However, they are often limited in effectiveness, primarily transferring contaminants between phases and incurring higher costs. In contrast, advanced oxidation processes (AOPs) have gained attention for the treatment of organic pollutants with low biodegradability. AOPs generate highly reactive oxygen species (ROS) in aqueous solutions, enabling the complete mineralization of pollutants and providing an efficient approach for their removal [4].

Traditional AOPs are often limited by the high cost of catalysts such as H_2O_2 and O_3, as well as the need for complex equipment, leading to elevated operational costs [5]. To address these challenges, photo-induced catalytic degradation has attracted significant attention. Photocatalytic dye degradation provides an efficient, energy-saving, and cost-effective method for breaking down dyes and organic contaminants into less harmful products [6]. Solar photocatalysis harnesses sunlight to activate photocatalysts, offering an environmentally sustainable approach to wastewater treatment. Upon light irradiation, photocatalysts generate electron-hole pairs that drive chemical reactions, ultimately leading to pollutant mineralization [7]. Consequently, the development of high-performance, efficient, and environmentally benign photocatalytic materials has become a central focus of research in this field. The reported photocatalytic efficiencies of different catalysts for MB degradation are summarized in **Table 1**.

Table 1. Overview of reported photocatalysts and their efficiencies toward MB degradation.

S. No.	Photocatalyst	Synthesis Method	Light source	Time (min.)	Degradation (%)	References
1.	TE-g-C_3N_4	Thermal exfoliation of bulk g-C_3N_4	UV	60	92	[8]
2.	Fe_3O_4/hTiO_2/g-C_3N_4	Reflux-precipitation and Sol-gel method	Xe lamp. 500 W	120	95	[9]
3.	1 $C^{-1}Fe_3O_4$/g-C_3N_4	Wet impregnation method.	Visible	180	92	[10]
4.	$ZnWO_4$/g-C_3N_4	Hydrothermal approach	Visible	120	92.9	[11]
5.	Zeolite-supported g-C_3N_4/ZnO/CeO_2	Solid-state method	visible	180	95.89	[12]
6.	Ag-Ag_2SeO_3/Ppy	Precipitation	Visible	25	90.51	[13]
7.	$BiVO_4$	Co-precipitation	sun light	80	86	[14]
8.	$La_{0.75}Ca_{0.25}MnO_3$	Wet chemical method	Visible	100	68.52	[15]
9.	CeO_2-NPs/GO/PAM	Polymerization	UV-A	90	90	[16]
10.	Fe/g-C_3N_4/rGO	Green Synthesis	Visible (100 W)	30	97.65	This work

Graphitic carbon nitride (g-C_3N_4) is a graphene-like 2D polymer composed of carbon and nitrogen atoms. It has attracted considerable attention as a visible-light-responsive photocatalyst due to its large surface area, high porosity, thermal and chemical stability, non-toxicity, low cost, and facile synthesis from abundant resources [1]. It is a metal-free, n-type semiconductor possessing a band gap around 2.97 eV [17]. However, g-C_3N_4 suffers from rapid electron-hole recombination, low selectivity, poor solar light absorption and weak redox capability, which limit its photocatalytic efficiency. To overcome these limitations, researchers have combined g-C_3N_4 with other functional materials, such as carbon-based materials, metal or metal oxide NPs, and co-catalysts, or employed doping and functionalization strategies [18].

Among carbon-based materials, graphene or reduced graphene oxide (rGO) has been widely used as a support to improve the photocatalytic activity of semiconductors. rGO possesses a unique two-dimensional honeycomb structure with outstanding electrical, optical, mechanical, and thermal properties. Incorporation of photoactive nanomaterials onto rGO sheets efficiently suppresses electron-hole recombination, allowing photogenerated electrons to participate in oxidative reactions and enhancing overall photocatalytic performance. Therefore, rGO serves as an excellent platform for supporting g-C_3N_4, facilitating charge transport, and improving photocatalytic efficiency [19].

Fe_3O_4 NPs are commonly employed in environmental remediation due to their high adsorption capacity, photocatalytic potential, abundance, low cost, low toxicity, notable catalytic activity and facile synthesis. When combined with g-C_3N_4 and rGO, Fe_3O_4 forms heterojunctions that enhance spatial charge separation, further reducing electron-hole recombination [20].

The integration of g-C_3N_4, rGO, and Fe_3O_4 into a single nanocomposite exploits the synergistic effects of each component: g-C_3N_4 serves as the primary photocata-

lyst generating electron-hole pairs under visible light, rGO enhances electron transport and suppresses charge recombination, and Fe_3O_4 promotes efficient charge separation at the heterojunction interface and provide more active sites. This interfacial synergy improves the photocatalytic efficiency while preserving the chemical stability and environmental compatibility of the g-C_3N_4 framework, resulting in a sustainable and high-performance photocatalyst system [21].

This study reports the synthesis and characterization of eco-friendly Fe_3O_4/g-C_3N_4/rGO nanocomposites as visible-light-responsive photocatalysts for the degradation of MB dye. The photocatalytic activity was evaluated under visible light by varying key parameters, including initial dye concentration, catalyst dosage and solution pH. The results demonstrate the effectiveness of Fe_3O_4/g-C_3N_4/rGO composites in enhancing visible-light-driven photocatalysis, offering a promising approach for mitigating dye pollution in aquatic environments.

2. Materials and Methods

2.1. Synthesis of Fe_3O_4 NPs through Green Tea Leaves Extract

Green tea extract was prepared by heating 4 g of tea leaves in 100 mL deionized water at 60˚C for 15 min, followed by filtration. For Fe_3O_4 synthesis, 0.811 g $FeCl_3$ was dissolved in 50 mL of the extract, sonicated for 1 h, and the resulting precipitate was filtered, washed with ethanol and deionized water, oven-dried at 70˚C, and ground into fine powder.

2.2. Synthesis of g-C_3N_4

The g-C_3N_4 was synthesized by heating 10 g of melamine in a covered crucible at 650˚C for 4 h, with a heating rate of 5˚C/min in air, followed by natural cooling, grinding, and storage [22].

2.3. Synthesis of GO

GO was synthesized using an improved Hummers' method. Briefly, 1 g graphite was mixed with H_2SO_4/H_3PO_4 (120:15 mL) under ice bath conditions (<5˚C), followed by slow addition of 6 g $KMnO_4$ and stirring for 30 min. The mixture was then heated to 35˚C and stirred for 12 h. After cooling, DI water was added while maintaining < 60˚C, and oxidation was terminated by adding H_2O_2. The product was filtered, washed with HCl (1:10) and DI water until neutral pH, air-dried for 5 - 6 days and ground into GO powder [23].

2.4. Synthesis of Fe_3O_4/g-C_3N_4/rGO Nanocomposites

The Fe_3O_4/g-C_3N_4/rGO nanocomposites were synthesized using green tea extracted Fe_3O_4 NPs, along with g-C_3N_4 and GO. To prepare the composite material, 0.2 g of GO was dispersed in 50 mL of extract and ultrasonicated for 15 min. Subsequently, 0.2 g of g-C_3N_4 was added to the solution, and the ultrasonication process was repeated for an additional 15 min. Following this, 0.8 g of $FeCl_3$ was introduced into the mixture, which was stirred at room temperature for 1 h. The

resulting mixture was then washed thoroughly with deionized (DI) water and ethanol before being dried in an oven at 80˚C for 4 h.

2.5. Characterization

The crystalline phases of synthesized NPs were examined using Rigaku make automated multipurpose X-ray diffractometer (model: SMARTLAB) in the 2θ range of 10˚ - 80˚ Surface functional groups of the synthesized NPs were analyzed using a FTIR spectrum 2 (PerkinElmer) with measurements recorded in the range 4000 - 400 cm^{-1}. UV-Vis diffusion reflectance spectra were acquired using Shimadzu UV-2600 to evaluate optical absorption properties. Surface morphology and elemental composition were characterized using filed emission scanning electron microscope (JEOL JSM-7610 F PLUS). The BET analysis was conducted using a NovaTouch LX2 gas sorption instrument (Quantachrome Instrument) to evaluate the specific surface area and pore size distribution. LC-MS analysis was conducted using a Waters Micromass Q-Tof Micro to investigate dye degradation. UV-Vis absorption spectra were acquired using an Agilent Carry 5000 spectrophotometer.

2.6. Photocatalytic Degradation of MB Dye

MB was employed as a model dye pollutant to assess the visible-light-driven photocatalytic activity of Fe_3O_4 and Fe_3O_4/g-C_3N_4/rGO. In a typical experiment, 10 mg of catalyst was dispersed in 50 mL of a 20 ppm MB solution contained in a 250 mL beaker. Experimental conditions, including solution pH, dye concentration, and catalyst dosage, were systematically optimized to achieve maximum degradation efficiency. Prior to irradiation with a 100 W visible light source, the suspension was stirred in the dark to establish adsorption-desorption equilibrium. At specific time intervals, 5 mL aliquots were withdrawn and centrifuged at 6000 rpm for 1 min to separate the photocatalyst. The concentration of MB was then monitored by recording UV-Vis absorption spectra at 617 nm. The photocatalytic degradation efficiency was calculated using the following expression [24].

$$C_{deg} = \frac{C_0 - C_t}{C_0} \times 100\% = \frac{A_0 - A_t}{A_0} \times 100\% \quad (1)$$

here C_0, C_t and A_0, A_t represent the concentrations (mg/L) and absorbance of MB dye at the initial time and at the time "t" respectively.

3. Results and Discussion

The XRD spectra of the Fe_3O_4/g-C_3N_4/rGO composite, as shown in **Figure 1**, exhibits distinct reflections that confirm the successful integration of the three components. A weak peak at 11.12˚ is indexed to the (001) plane of GO, indicating the presence of partially oxidized graphitic domains that were not completely reduced during synthesis. The broad feature around 22˚ corresponds to the (002) plane of reduced graphene oxide (rGO), typically associated with disordered graphitic layers and amorphous carbon phases [25] [26]. The diffraction peak at 12.88˚ is due to g-C_3N_4 (100), while the strong peak at 28.0˚ corresponds to the (002) plane of

g-C_3N_4 [27]. Additional reflections at 31.73˚, 42.70˚, and 57.72˚ are corresponding to the (220), (400), and (511) planes of Fe_3O_4 NPs, although the most intense Fe_3O_4 (311) reflection at 35.4˚ is suppressed, likely due to low oxide loading, nanoscale broadening, or overlap with the carbonaceous background. The Fe_3O_4 peaks also appear diminished, indicating poor crystallinity and fine dispersion within the composite [28]. These observations collectively validate the coexistence of g-C_3N_4, rGO, Fe_3O_4 and highlight strong structural interactions among them, confirming the successful synthesis of the ternary composite. The crystallite size of the NPs was calculated using the Debye-Scherrer equation.

$$D = \frac{0.9\lambda}{\beta\cos\theta} \tag{2}$$

where D is the crystallite size, λ is the X-ray wavelength (1.54060 Å), β is the full width at half maximum (FWHM), and θ is the Bragg angle of the diffraction peak. Based on this analysis, the average crystallite size of the Fe_3O_4/g-C_3N_4/rGO nanocomposites was estimated to be 58.5 nm from the (002) reflection, as summarized in Table 2.

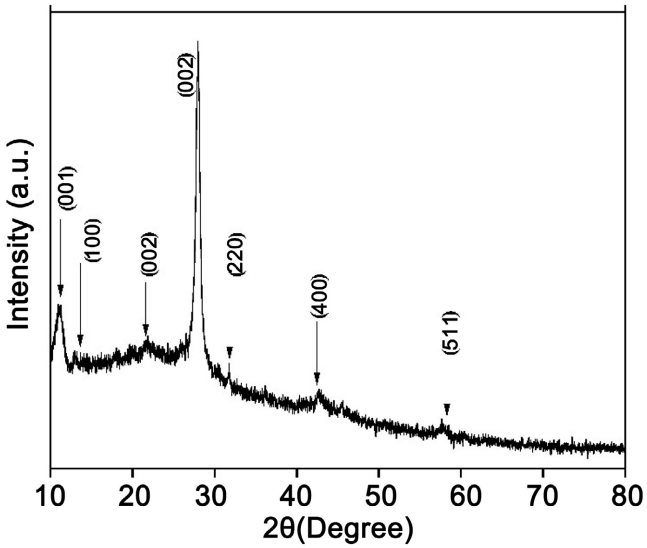

Figure 1. XRD spectra of Fe_3O_4/g-C_3N_4/rGO nanocomposites.

Table 2. Experimental XRD data of Fe_3O_4/g-C_3N_4/rGO nanocomposites.

Sample	Peak	Position (˚2θ)	FWHM (˚2θ)	d-spacing (A˚)	Crystallite size (nm)
rGO	(001)	11.12	0.81	7.94	
	(002)	21.80	0.0010	4.07	
g-C_3N_4	(100)	12.8806	0.62	6.87	
	(002)	28.0000	0.14	3.18	58.5
Fe_3O_4	(220)	31.7362	0.14	2.81	
	(400)	42.7090	0.15	2.12	
	(511)	57.7200	0.1	1.60	

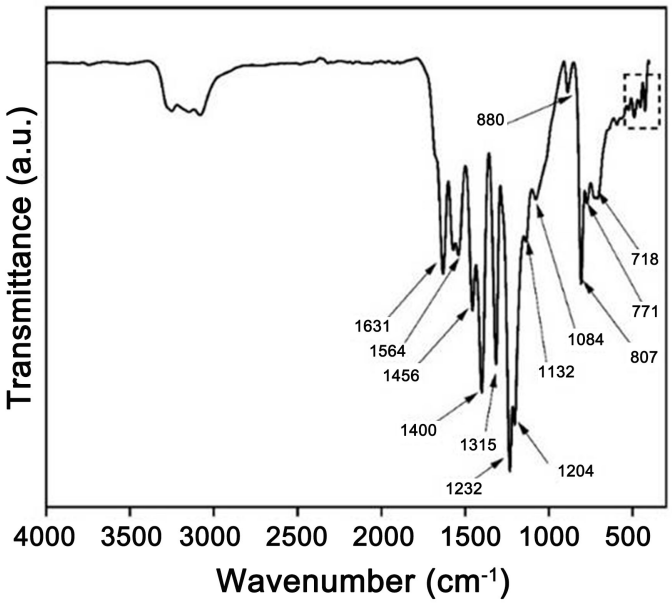

Figure 2. FTIR analysis of Fe_3O_4/g-C_3N_4/rGO nanocomposites.

The FTIR spectrum of the Fe_3O_4/g-C_3N_4/rGO composites (**Figure 2**) displays characteristic vibrational features corresponding to all three components. A broad absorption band in the 3000 - 3300 cm^{-1} region is attributed to O-H and N-H stretching, associated with surface hydroxyl and amine groups [29]. Peaks at 1631, 1564, 1456, 1400, and 1315 cm^{-1} correspond to C=N and C-N stretching, as well as aromatic skeletal vibrations from the g-C_3N_4 framework and residual functional groups on rGO [30]. In the 1200 - 1000 cm^{-1} region, bands at 1204, 1132, and 1084 cm^{-1} are assigned to C-N and C-O stretching modes. A sharp peak at 807 cm^{-1} confirms the presence of triazine ring bending vibrations. The peak at 718 cm^{-1} is likely due to N-H wagging or ring deformation. Notably, multiple bands between 500 and 400 cm^{-1} are attributed to Fe-O stretching vibrations, indicating the incorporation of Fe_3O_4 [30]. The spectrum confirms the successful formation of the composite, with all components interacting through non-covalent interactions without structural degradation [29].

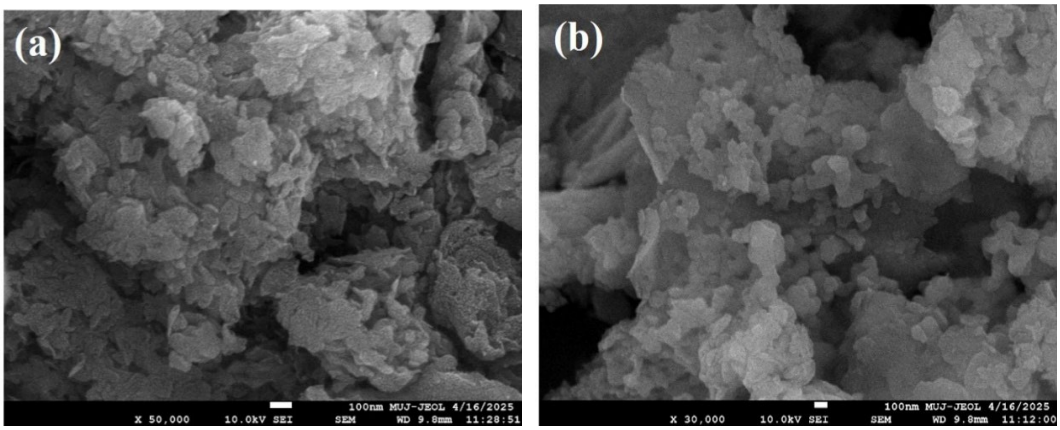

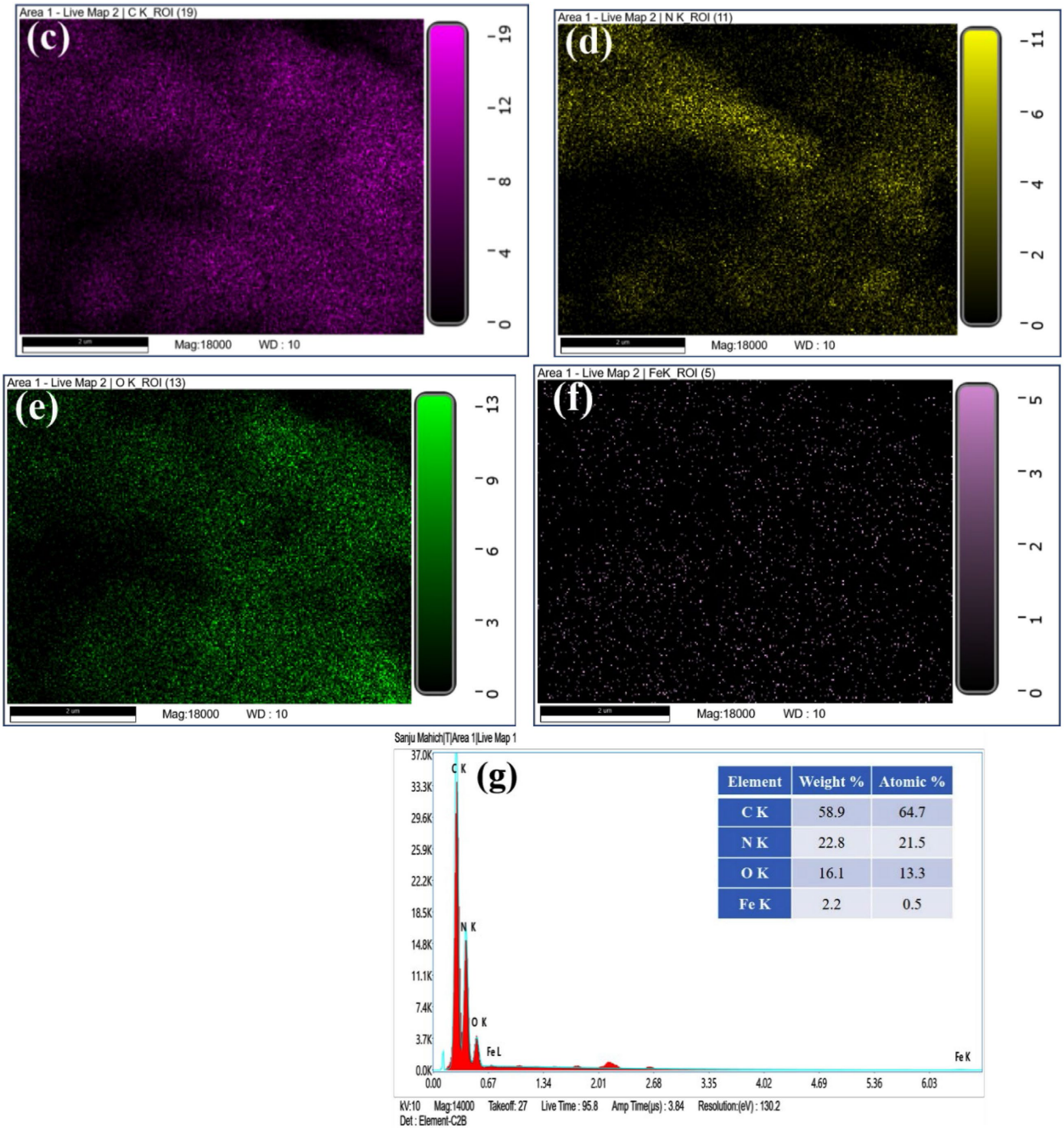

Figure 3. (a - b) FESEM micrographs of the Fe_3O_4/g-C_3N_4/rGO nanocomposites (c - f) elemental distribution maps for carbon (C), nitrogen (N), oxygen (O), and iron (Fe), respectively (g) EDS spectrum of the Fe_3O_4/g-C_3N_4/rGO nanocomposites.

FESEM images of the Fe_3O_4/g-C_3N_4/rGO composite (**Figure 3(a)**, **Figure 3(b)**) display a wrinkled, sheet-like layered morphology characteristic of g-C_3N_4 and rGO. The introduction of rGO increases surface roughness and sheet separation, providing favorable sites for the uniform dispersion of Fe_3O_4 nanoparticles (NPs). The fine granular structures observed on the surface correspond to Fe_3O_4 NPs anchored within the matrix. EDS as shown in **Figure 3(g)** confirmed the presence of Fe (2.2 wt%), while elemental mapping (**Figures 3(c)-(f)**) revealed a homoge-

neous distribution of Fe, C, N and O throughout the composite. These findings confirm the successful incorporation of Fe_3O_4 NPs without noticeable aggregation, ensuring uniform integration of all components while maintaining the layered structure.

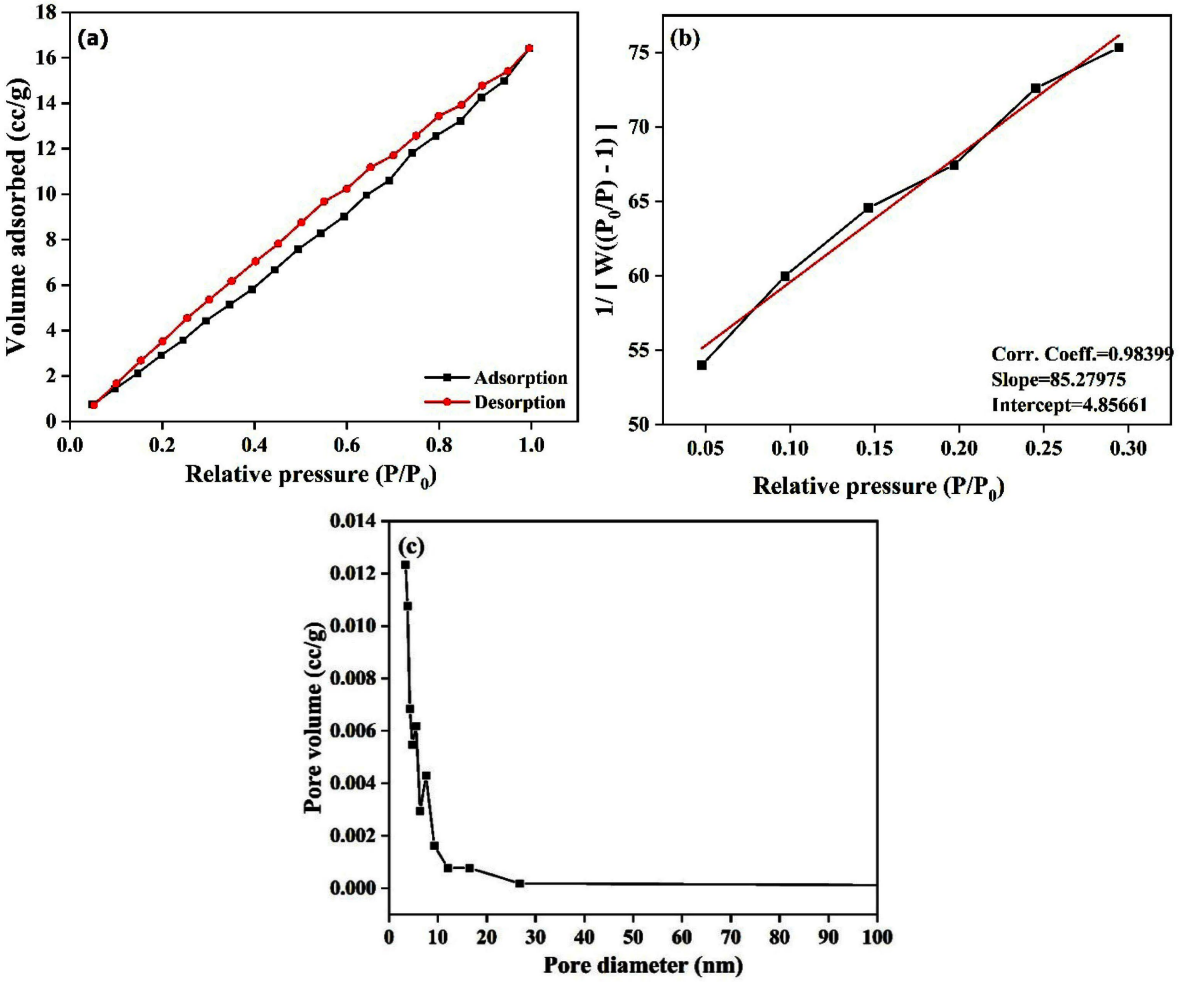

Figure 4. (a) N_2 adsorption-desorption isotherm (b) BET analysis for surface area estimation and (c) BJH pore size distribution curve of Fe_3O_4/g-C_3N_4/rGO nanocomposites.

Nitrogen adsorption-desorption analysis was performed to study the pore characteristics and surface area of the Fe_3O_4/g-C_3N_4/rGO ternary nanocomposite. The isotherm (**Figure 4(a)**) exhibited a type IV curve with an H3 hysteresis loop, as classified by IUPAC, which is typical of mesoporous materials with slit-like pores arising from layered structures such as rGO and g-C_3N_4. The BET plot ($1/[W(P_0/P) - 1]$ vs. P/P_0) in the relative pressure range of 0.05 - 0.3 showed excellent linearity (R^2 = 0.98399), confirming the accuracy of the surface area estimation (**Figure 4(b)**).

The calculated BET surface area of the nanocomposite was 25.546 m^2/g, indicating the availability of sufficient active surface sites. The average pore volume and diameter, obtained from BJH analysis, were 0.0236102 cc/g and 3.37 nm, respectively, which further confirm its mesoporous nature.

The BJH pore size distribution curve (**Figure 4(c)**) revealed a broad range of pores with higher intensity in the lower pore diameter region, signifying abundant narrow mesopores and interparticle voids. These mesoporous features, coupled with the moderate surface area, are beneficial for photocatalysis as they enhance dye diffusion and adsorption at reactive sites [31].

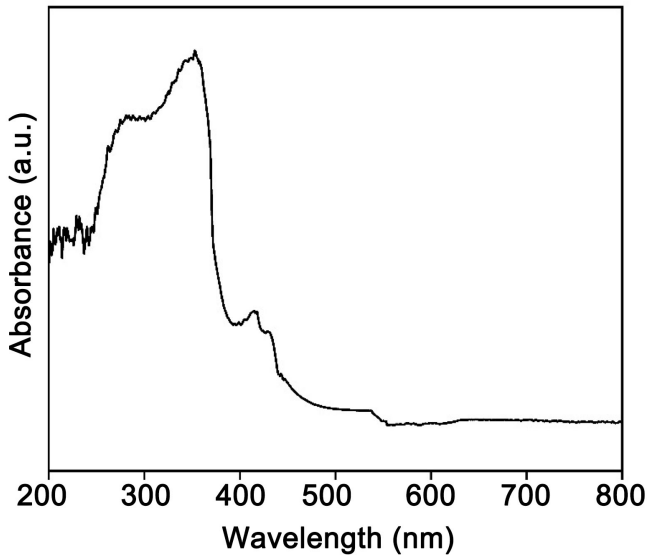

Figure 5. UV-DRS spectra of synthesized Fe_3O_4/g-C_3N_4/rGO nanocomposites.

The optical absorption properties of the Fe_3O_4/g-C_3N_4/rGO nanocomposites were investigated using UV-DRS (**Figure 5**). The spectrum exhibits a shoulder peak at 274 nm, attributed to $\pi \rightarrow \pi^*$ transitions of the aromatic C=C bonds in the rGO sheets [32]. The absorption peak at ~350 nm corresponds to the $\pi \rightarrow \pi^*$ transitions in g-C_3N_4 [33]. Moreover, adjacent absorption at 415 - 430 nm is observed, which are associated with Fe_3O_4 nanoparticles. The broad absorption can be ascribed to the synergistic effect of Fe_3O_4 NPs and rGO sheets interacting with the g-C_3N_4 matrix, thereby improving the light-harvesting potential of the composite. This enhancement promotes the generation of more photoinduced charge carriers under visible irradiation, which contributes to its high photocatalytic performance [34].

3.1. Photocatalytic Degradation Analysis

Control studies confirmed that MB remained stable in both light and dark conditions in the absence of a catalyst, showing negligible self-degradation. **Figure 6(a)**, **Figure 6(b)** display the UV-Vis absorption spectra of MB recorded at different irradiation times in the presence of Fe_3O_4/g-C_3N_4/rGO, where a gradual decrease in the absorption peak intensity is observed with increasing exposure duration. The corresponding degradation efficiencies are summarized in **Table 3** and plotted in **Figure 6(c)**, further demonstrating the superior activity of the ternary composite. The visible fading of MB during the degradation process is shown in **Figure 6(d)**.

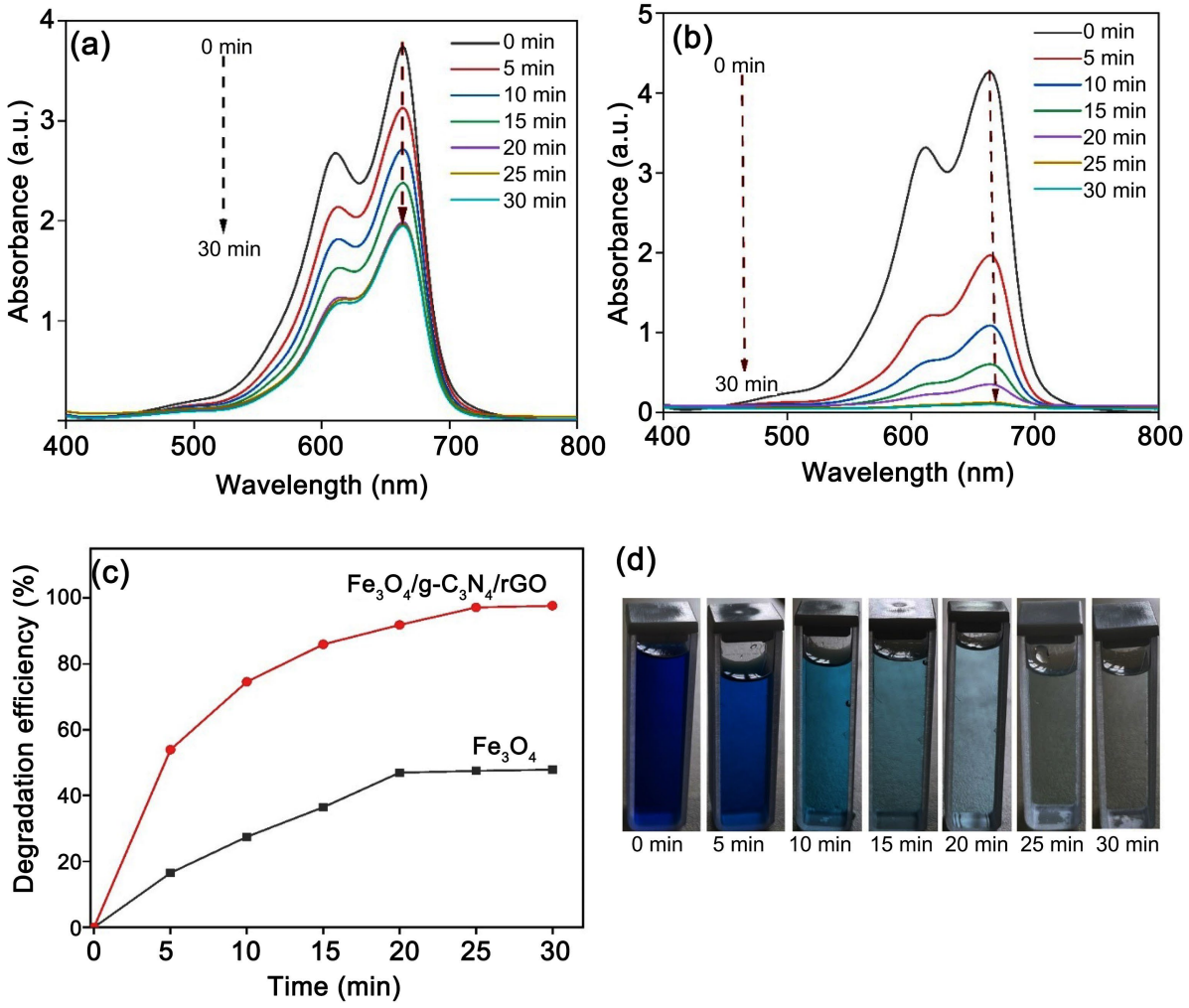

Figure 6. Time dependent UV-vis. absorption spectra of MB dye with (a) Fe_3O_4 (b) Fe_3O_4/g-C_3N_4/rGO nanocomposites and (c) calculated photocatalytic degradation efficiency of MB dye under visible light (d)visual demonstration of MB dye decolorization over time using Fe_3O_4/g-C_3N_4/rGO nanocomposites.

Fe_3O_4 NPs achieved a degradation efficiency of 47.86% within 30 min, whereas the Fe_3O_4/g-C_3N_4/rGO nanocomposites showed a much higher efficiency of 97.65% under the same conditions. The relatively low activity of Fe_3O_4 can be explained by its small surface area, low electrical conductivity, short hole diffusion length, and rapid electron-hole recombination, all of which limit the formation of ROS such as hydroxyl radicals (OH•) and superoxide anions (O_2^-) that are required for dye degradation [35]. In contrast, the ternary Fe_3O_4/g-C_3N_4/rGO composite exhibits markedly enhanced photocatalytic activity due to the synergistic interactions among its constituents, which increases surface area and promotes efficient charge separation, thereby enhancing electron-hole pair generation and transfer [36]. It is well established that pristine g-C_3N_4 alone suffers from fast charge carrier recombination and limited visible-light utilization, which restrict its photocatalytic performance [1]. Incorporation of rGO provides an efficient electron-accepting and transporting pathway, thereby suppressing recombination and ac-

celerating electron transfer for redox reactions [37]. Simultaneously, Fe_3O_4 nanoparticles act as electron mediators, promoting charge separation and extending light absorption [20]. Furthermore, the formation of heterojunction interfaces facilitates directional charge migration and sustains continuous ROS production, ultimately resulting in efficient methylene blue degradation [38] [39].

Table 3. MB dye degradation efficiency (%) using Fe_3O_4 and Fe_3O_4/g-C_3N_4/rGO nanocomposites.

% Photodegradation of MB dye		
Time (min)	**Fe_3O_4**	**Fe_3O_4/g-C_3N_4/rGO**
5	16.49	53.92
10	27.48	74.54
15	36.44	85.92
20	46.94	91.83
25	47.51	97.13
30	47.86	97.65

3.2. Photocatalytic Degradation Pathway

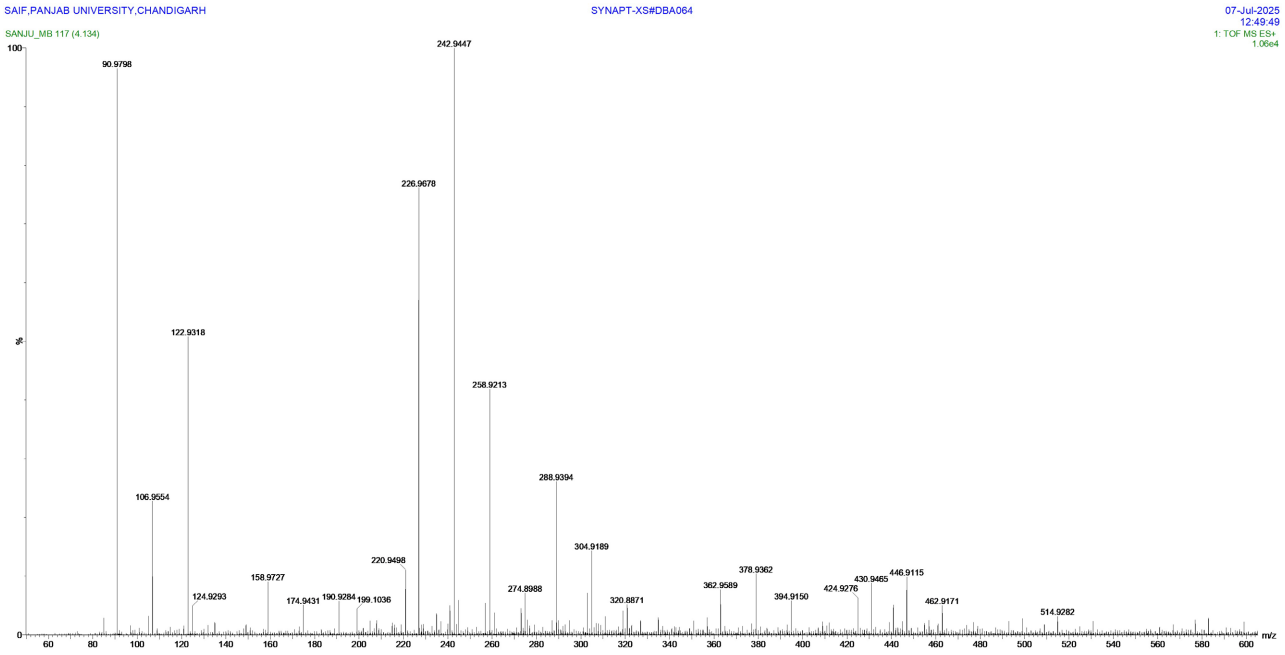

Figure 7. LC-MS spectra of MB dye during photocatalytic degradation using Fe_3O_4/g-C_3N_4/rGO nanocomposites.

The photocatalytic degradation of MB using Fe_3O_4/g-C_3N_4/rGO nanocomposites under visible light was investigated through LC-MS analysis. The spectra (**Figure 7**) revealed distinct m/z peaks at 318, 303, 257, 243, 229, 200, 159, 124, and 93, along with the disappearance of the parent MB m/z peak at 284. This observation confirms that MB molecules undergo progressive decomposition into smaller in-

termediates. The detected fragments indicate that the degradation pathway involves successive demethylation steps, disruption of the aromatic structure, and further oxidation. The proposed mechanism (**Figure 8**) illustrates the gradual transformation of MB into low-molecular-weight intermediates, ultimately leading to complete mineralization into CO_2 and H_2O [40] [41]. These findings confirm that ROS predominantly govern the photocatalytic degradation mechanism.

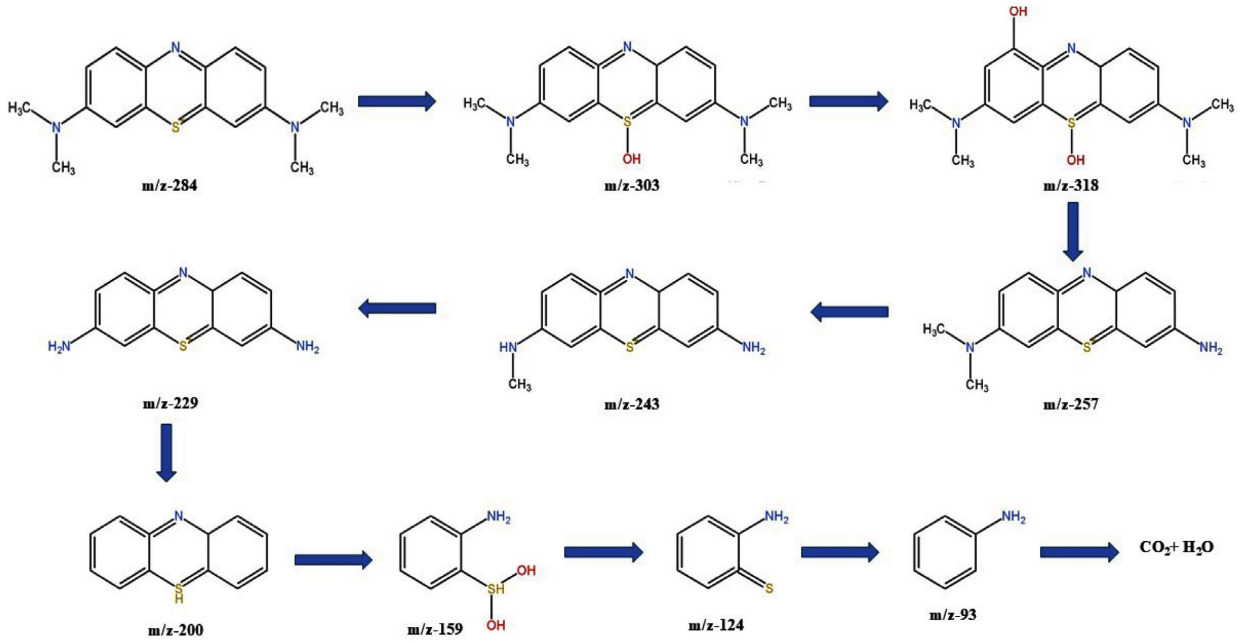

Figure 8. Proposed photocatalytic degradation pathway of MB with Fe_3O_4/g-C_3N_4/rGO nanocomposites.

3.3. Factors Affecting the Photocatalytic Degradation of MB Dye

3.3.1. Effect of Catalyst Loading

To determine the optimum catalyst dosage for MB dye degradation, experiments were performed by varying the amount of Fe_3O_4/g-C_3N_4/rGO nanocomposite. At an initial dye concentration of 20 ppm and optimized pH under visible light, catalyst dosages of 5, 10, and 15 mg were evaluated, achieving degradation efficiencies of 80.26%, 97.65%, and 97.87% within 30 min, respectively (**Figure 9(a)**). The results show that increasing the catalyst loading enhances degradation up to a certain level, owing to the greater availability of active sites that accelerate dye adsorption and photodegradation. However, beyond the optimal dosage of 10 mg, only marginal improvement was observed. This slight decline in efficiency can be attributed to particle agglomeration at higher concentrations, which decreases the effective surface area, restricts access to active sites, and increases light scattering, thereby limiting photon penetration and suppressing the generation of ROS [42], [43]. Thus, optimizing catalyst dosage is essential to balance active site availability and light utilization, ensuring maximum photocatalytic efficiency while avoiding the drawbacks of excessive loading.

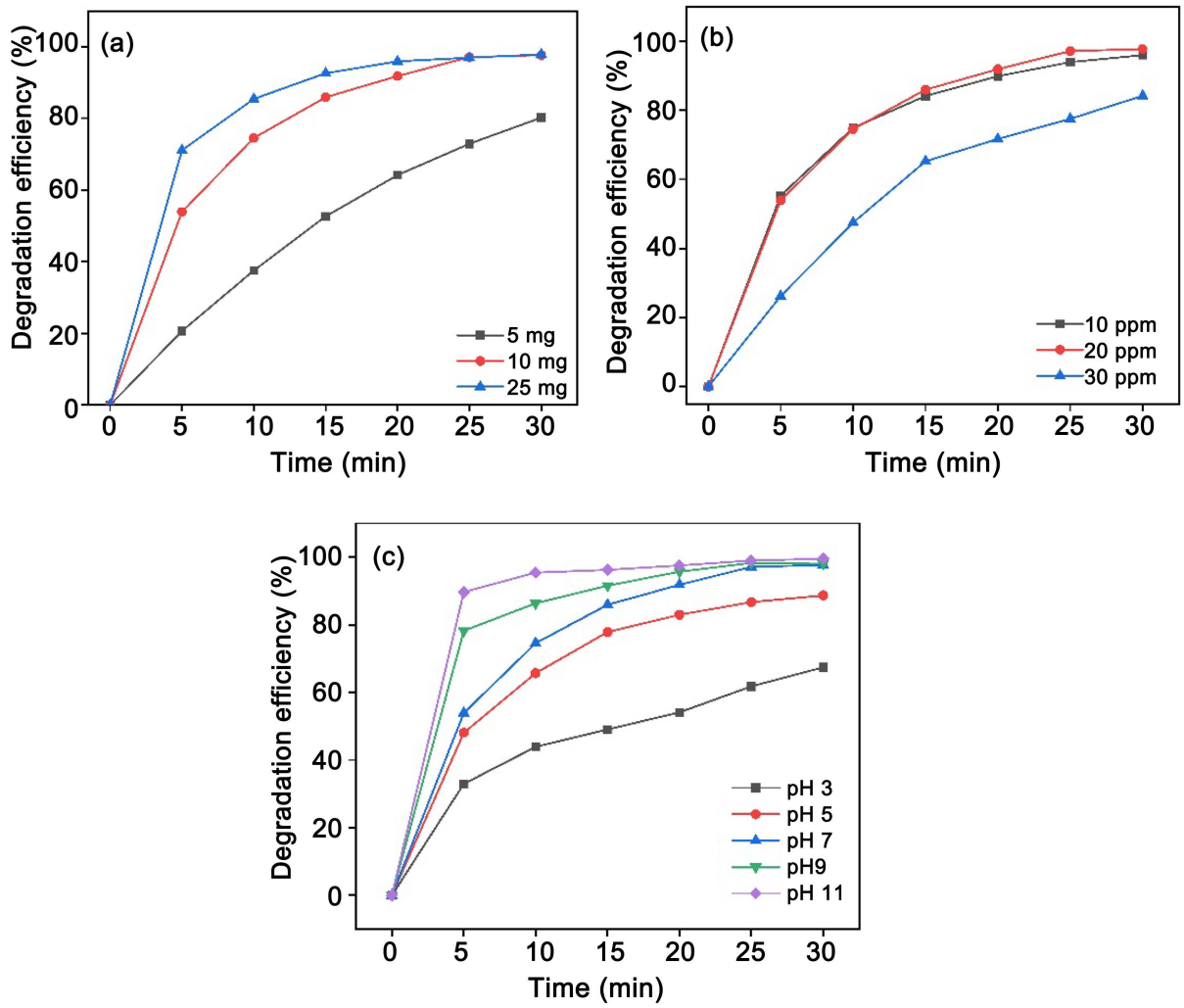

Figure 9. Variation in MB dye degradation efficiency over time using Fe_3O_4/g-C_3N_4/rGO nanocomposites under different conditions: (a) catalyst dosage, (b) initial dye concentration, and (c) pH values.

3.3.2. Effect of Dye Concentration

The initial concentration of the dye is a key factor influencing photocatalytic performance. To assess this parameter, MB solutions with concentrations of 10, 20, and 30 ppm were treated using 10 mg of Fe_3O_4/g-C_3N_4/rGO catalyst in 50 mL solution under visible light at the optimized pH. After 30 min of irradiation, the degradation efficiencies were 95.89%, 97.65%, and 84.17%, respectively, with 20 ppm showing the highest efficiency and therefore selected as the optimum concentration for subsequent studies (**Figure 9(b)**). At lower concentrations, the limited availability of dye molecules results in insufficient adsorption, leaving many active sites unoccupied. At moderate concentrations, a balance between dye availability and catalyst active sites enhances adsorption and degradation efficiency [44]. However, at higher concentrations, excessive dye molecules saturate the catalyst surface, while the increased optical density restricts photon penetration, thereby suppressing the generation of ROS and reducing overall photocatalytic activity [45]. These findings underline the necessity of optimizing the initial dye concentration to achieve

maximum degradation efficiency.

3.3.3. Effect of pH

The pH of the dye solution is a crucial parameter governing photocatalytic degradation, as it influences both the surface charge of the photocatalyst and the ionization state of dye molecules. To examine this effect, the Fe_3O_4/g-C_3N_4/rGO nanocomposite was tested for the pH-dependent degradation of cationic MB dye (20 ppm, 10 mg catalyst). The degradation efficiency increased progressively with pH, achieving 67.40%, 88.68%, 97.65%, 98.00%, and 99.53% at pH 3, 5, 7, 9, and 11, respectively, after 30 min of visible-light irradiation (**Figure 9(c)**). The enhanced activity in alkaline media can be ascribed to two main factors: 1) strong electrostatic attraction between positively charged MB molecules and the negatively charged catalyst surface (due to rGO and g-C_3N_4), and 2) favorable generation of ROS such as OH• and O_2^-, which accelerate oxidative degradation reactions [46]-[48]. These findings emphasize the significance of pH optimization according to the ionic characteristics of the target pollutant to achieve maximum photocatalytic performance of Fe_3O_4/g-C_3N_4/rGO nanocomposites.

3.4. Reusability

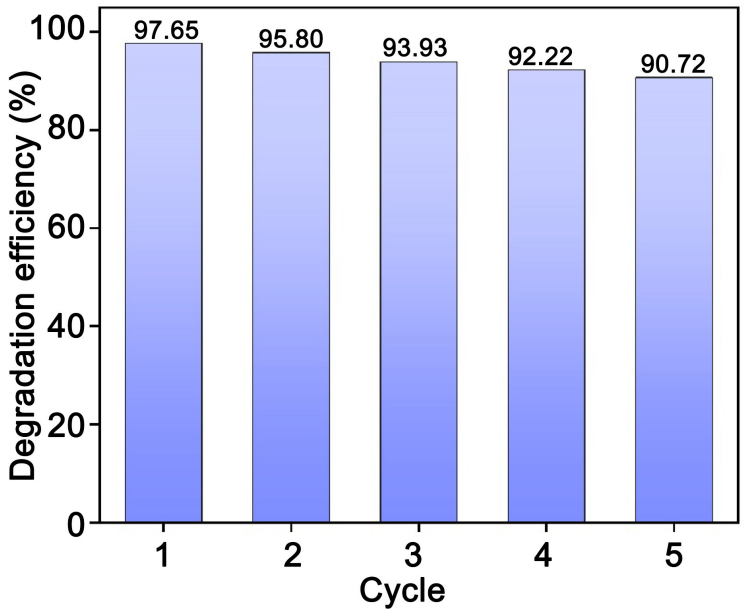

Figure 10. MB dye degradation efficiency (%) over successive photocatalytic runs using Fe_3O_4/g-C_3N_4/rGO nanocomposites.

The long-term reusability of a photocatalyst is an essential parameter for its practical deployment in environmental remediation. To evaluate this, the Fe_3O_4/g-C_3N_4/rGO nanocomposite was tested under optimized conditions (20 ppm dye, 10 mg catalyst, pH 7) for five consecutive cycles. After each run, the photocatalyst was collected by centrifugation, thoroughly washed with deionized water and ethanol, dried, and reused under identical conditions. Following 30 min of visible-

light irradiation, the degradation efficiencies were recorded as 97.65%, 95.80%, 93.93%, 92.22%, and 90.72% for the 1st to 5th cycle, respectively (**Figure 10**), indicating only a modest decline of ~7%. The slight reduction in activity can be attributed to the deposition of intermediate by-products on the catalyst surface, which may partially block active sites, as well as minor material loss during recovery and washing steps [49] [50]. Overall, the nanocomposite exhibited excellent durability and recyclability, confirming its strong potential for sustained and efficient dye degradation under visible light.

4. Conclusion

This work reports the successful fabrication and application of Fe_3O_4/g-C_3N_4/rGO ternary nanocomposites as efficient visible-light-driven photocatalysts for the degradation of MB dye in aqueous solution. The nanocomposites were synthesized via a simple route using melamine-derived g-C_3N_4, rGO nanosheets and Fe_3O_4 NPs. In this hybrid system, g-C_3N_4 served as the primary photocatalytic matrix, rGO functioned as a conductive network enabling fast electron transport, while Fe_3O_4 NPs provided additional active sites and enhanced interfacial charge transfer. Structural and morphological characterizations confirmed the successful integration of all components, uniform distribution, and a mesoporous framework with a surface area of 25.55 m^2/g and an average pore diameter of 3.37 nm. Photocatalytic studies demonstrated that the ternary nanocomposite displayed significantly higher degradation activity than its individual constituents, owing to the synergistic interactions facilitating effective charge separation and migration. Under optimized conditions, the material achieved 99.53% MB degradation within 30 min at pH 11, while maintaining high efficiency (97.65%) even under neutral pH, highlighting its practical potential. In addition, the photocatalyst retained 90.72% efficiency after five consecutive runs, indicating excellent reusability and stability. Overall, Fe_3O_4/g-C_3N_4/rGO emerges as a durable, sustainable, and cost-effective photocatalyst for visible-light-assisted wastewater remediation. Moreover, future research may focus on optimizing large-scale synthesis and evaluating performance in complex real wastewater systems to assess its practical feasibility for industrial applications.

Funding

The authors declare that no funds, grants, or other support were received during the preparation of this manuscript.

Authors' Contributions

Sanju Mahich: Conceptualization, Methodology, Writing-original draft. **Kundan Singh Shekhawat:** Investigation, Methodology. **Shubham Gupta**: Data analysis. **Anuj Kumar**: Validation, Visualization. **Sanjay Kumar Swami**: Writing - review & editing, Validation. **Jaya Mathur**: Methodology, Supervision, Investigation. **Vijay Devra**: Supervision. **Amanpal Singh**: Conceptualization, Writing - review & editing, Supervision.

Ethical Approval

Authors have read all the ethics carefully to publish and agree with the terms and conditions of the journal.

Consent to Participate

Not applicable

Consent to Publish

The authors give their consent to publish the manuscript in this journal after acceptance.

Data Availability Statement

All data supporting the findings of this study are included within the article.

Acknowledgements

The authors express their sincere gratitude to Manipal University Jaipur and Malaviya National Institute of Technology (MNIT), Jaipur, Rajasthan, India, for providing access to characterization facilities.

Conflicts of Interest

The authors have no relevant financial or non-financial interests to disclose.

References

[1] Guo, R., Wang, J., Bi, Z., Chen, X., Hu, X. and Pan, W. (2022) Recent Advances and Perspectives of g-C_3N_4-Based Materials for Photocatalytic Dyes Degradation. *Chemosphere*, **295**, Article 133834. https://doi.org/10.1016/j.chemosphere.2022.133834

[2] Kumari, H., Sonia,, Suman,, Ranga, R., Chahal, S., Devi, S., *et al.* (2023) A Review on Photocatalysis Used for Wastewater Treatment: Dye Degradation. *Water, Air, & Soil Pollution*, **234**, 1-46. https://doi.org/10.1007/s11270-023-06359-9

[3] Dutta, S., Adhikary, S., Bhattacharya, S., Roy, D., Chatterjee, S., Chakraborty, A., *et al.* (2024) Contamination of Textile Dyes in Aquatic Environment: Adverse Impacts on Aquatic Ecosystem and Human Health, and Its Management Using Bioremediation. *Journal of Environmental Management*, **353**, Article 120103. https://doi.org/10.1016/j.jenvman.2024.120103

[4] Babu Ponnusami, A., Sinha, S., Ashokan, H., V Paul, M., Hariharan, S.P., Arun, J., *et al.* (2023) Advanced Oxidation Process (AOP) Combined Biological Process for Wastewater Treatment: A Review on Advancements, Feasibility and Practicability of Combined Techniques. *Environmental Research*, **237**, Article 116944. https://doi.org/10.1016/j.envres.2023.116944

[5] Iyyappan, J., Gaddala, B., Gnanasekaran, R., Gopinath, M., Yuvaraj, D. and Kumar, V. (2024) Critical Review on Wastewater Treatment Using Photo Catalytic Advanced Oxidation Process: Role of Photocatalytic Materials, Reactor Design and Kinetics. *Case Studies in Chemical and Environmental Engineering*, **9**, Article 100599. https://doi.org/10.1016/j.cscee.2023.100599

[6] Hitam, C.N.C. and Jalil, A.A. (2020) A Review on Exploration of Fe_2O_3 Photocatalyst Towards Degradation of Dyes and Organic Contaminants. *Journal of Environmental Management*, **258**, Article 110050. https://doi.org/10.1016/j.jenvman.2019.110050

[7] Roy, J.S. and Messaddeq, Y. (2024) The Role of Solar Concentrators in Photocatalytic Wastewater Treatment. *Energies*, **17**, Article 4001. https://doi.org/10.3390/en17164001

[8] Ganesan, S., Kokulnathan, T., Sumathi, S. and Palaniappan, A. (2024) Efficient Photocatalytic Degradation of Textile Dye Pollutants Using Thermally Exfoliated Graphitic Carbon Nitride (TE-g-C_3N_4). *Scientific Reports*, **14**, Article No. 2284. https://doi.org/10.1038/s41598-024-52688-y

[9] Li, X., Zhang, W., Wen, X., You, L. and Li, J. (2023) Construction of Magnetically Recyclable Fe_3O_4/hTiO_2/g-C_3N_4 Composites for Solar Photocatalytic Degradation of Organic Pollutants: Study on the Performance and Mechanism Insight. *Journal of Molecular Liquids*, **392**, Article 123498. https://doi.org/10.1016/j.molliq.2023.123498

[10] Ishak, N., Martynek, D., Velu, J., Bleha, R., Galář, P. and Šoóš, M. (2023) Revolutionizing Photocatalytic Water Treatment: An In-Depth Exploration of g-C_3N_4 Iron Oxide and Carbon-Mediated Upgrading for an Optimal Decontamination of Vltava River Water. *Colloids and Surfaces A*: *Physicochemical and Engineering Aspects*, **677**, Article 132292. https://doi.org/10.1016/j.colsurfa.2023.132292

[11] Barveen, N.R., Parasuraman, B., Wang, P., Zeng, C., Cheng, Y. and Thangavelu, P. (2024) Facile Construction of $ZnWO_4$/g-C_3N_4 Heterojunction for the Improved Photocatalytic Degradation of MB, RhB and Mixed Dyes. *Surfaces and Interfaces*, **53**, Article 105039. https://doi.org/10.1016/j.surfin.2024.105039

[12] Girma, S., Taddesse, A.M., Bogale, Y. and Bezu, Z. (2023) Zeolite-Supported g-C_3N_4/ZnO/CeO_2 Nanocomposite: Synthesis, Characterization and Photocatalytic Activity Study for Methylene Blue Dye Degradation. *Journal of Photochemistry and Photobiology A*: *Chemistry*, **444**, Article 114963. https://doi.org/10.1016/j.jphotochem.2023.114963

[13] Moosaviyan, S.A., Baezzat, M.R., Ghaedi, M. and Abbasi-Asl, H. (2023) Photocatalytic Decomposition of Methylene Blue and Rhodamine B Using Ag-Ag_2SeO_3/Ppy Nano-Photocatalyst from Aqueous Solutions: Experimental Design Optimization. *Journal of Nanostructure in Chemistry*, **14**, 419-436. https://doi.org/10.1007/s40097-023-00531-7

[14] Panda, P.K., Pattanaik, R., Mishra, S., Pradhan, D. and Kumar Dash, S. (2023) Superior Photocatalytic Degradation of MB Dye Using $BiVO_4$ Nanoparticles under Solar Light Irradiation. *Materials Today*: *Proceedings*. https://doi.org/10.1016/j.matpr.2023.11.039

[15] Nayak, H. and Padhi, B. (2023) Degradation of Methylene Blue Using Ca-Doped $LaMnO_3$ as a Photocatalyst under Visible Light Irradiation. *Results in Chemistry*, **6**, Artilce 101104. https://doi.org/10.1016/j.rechem.2023.101104

[16] Kalaycıoğlu, Z., Özuğur Uysal, B., Pekcan, Ö. and Erim, F.B. (2023) Efficient Photocatalytic Degradation of Methylene Blue Dye from Aqueous Solution with Cerium Oxide Nanoparticles and Graphene Oxide-Doped Polyacrylamide. *ACS Omega*, **8**, 13004-13015. https://doi.org/10.1021/acsomega.3c00198

[17] Alshamkhani, M.T., Putri, L.K., Lahijani, P., Lee, K.T. and Mohamed, A.R. (2023) A Metal-Free Electrochemically Exfoliated Graphene/Graphitic Carbon Nitride Nanocomposite for CO_2 Photoreduction to Methane under Visible Light Irradiation. *Journal of Environmental Chemical Engineering*, **11**, Article 109086. https://doi.org/10.1016/j.jece.2022.109086

[18] Ren, X., Guo, M., Xue, L., Xu, L., Li, L., Yang, L., *et al.* (2023) Photoelectrochemical Performance and S-Scheme Mechanism of Ternary Go/g-C_3N_4/TiO_2 Heterojunction Photocatalyst for Photocatalytic Antibiosis and Dye Degradation under Visible Light. *Applied Surface Science*, **630**, Article 157446. https://doi.org/10.1016/j.apsusc.2023.157446

[19] Anegbe, B., Ifijen, I.H., Maliki, M., Uwidia, I.E. and Aigbodion, A.I. (2024) Graphene Oxide Synthesis and Applications in Emerging Contaminant Removal: A Comprehensive Review. *Environmental Sciences Europe*, **36**, Article No. 15. https://doi.org/10.1186/s12302-023-00814-4

[20] Liu, M., Ye, Y., Ye, J., Gao, T., Wang, D., Chen, G., *et al.* (2023) Recent Advances of Magnetite (Fe_3O_4)-Based Magnetic Materials in Catalytic Applications. *Magnetochemistry*, **9**, Article 110. https://doi.org/10.3390/magnetochemistry9040110

[21] Luo, J., Dai, Z., Feng, M., Gu, M. and Xie, Y. (2023) Graphitic Carbon Nitride/Ferroferric Oxide/Reduced Graphene Oxide Nanocomposite as Highly Active Visible Light Photocatalyst. *Nano Research*, **16**, 371-376. https://doi.org/10.1007/s12274-022-5110-z

[22] Bharathkumar, S., Murugan, A., Cordero, M.A.W., Muthamizh, S., Ganesh, K., Rashid, N.A., *et al.* (2024) Z-Scheme Configured Iron Oxide/g-C_3N_4 Nanocomposite System for Solar-Driven H_2 Production through Water Splitting. *Applied Catalysis O: Open*, **190**, Article 206915. https://doi.org/10.1016/j.apcato.2024.206915

[23] Mahich, S., Saini, Y.K., Devra, V., *et al.* (2024) Metal-Free Adsorption and Photodegradation Methods for Methylene Blue Dye Removal Using Different Reduction Grades of Graphene Oxide. *Heliyon*, **10**, e31702. https://www.cell.com/heliyon/fulltext/S2405-8440(24)07733-8?uuid=uuid%3Ad3e2565f-9e28-40c6-bf95-498870bb8ee6

[24] Devi, K.N., Devi, S.A., Singh, W.J. and Singh, K.J. (2021) Nickel Doped Zinc Oxide with Improved Photocatalytic Activity for Malachite Green Dye Degradation and Parameters Affecting the Degradation. *Journal of Materials Science: Materials in Electronics*, **32**, 8733-8745. https://doi.org/10.1007/s10854-021-05545-x

[25] Liu, Y., Ma, L. and Chen, Y. (2018) A Simple One-Step Approach for Preparing Flexible rGO-MnO_2 Electrode Material. *Journal of Materials Science: Materials in Electronics*, **29**, 17438-17444. https://doi.org/10.1007/s10854-018-9843-0

[26] Some, S., Kim, Y., Yoon, Y., Yoo, H., Lee, S., Park, Y., *et al.* (2013) High-Quality Reduced Graphene Oxide by a Dual-Function Chemical Reduction and Healing Process. *Scientific Reports*, **3**, Article No. 1929. https://doi.org/10.1038/srep01929

[27] Liu, D., Yao, J., Chen, S., Zhang, J., Li, R. and Peng, T. (2022) Construction of rGO-Coupled C_3N_4/C_3N_5 2D/2D Z-Scheme Heterojunction to Accelerate Charge Separation for Efficient Visible Light H_2 Evolution. *Applied Catalysis B: Environmental*, **318**, Article 121822. https://doi.org/10.1016/j.apcatb.2022.121822

[28] Zang, X., Chang, Q., Liang, W., Wu, T., Wang, C. and Wang, Z. (2017) Micro-Solid Phase Extraction of Chlorophenols Using Reduced Graphene Oxide Functionalized with Magnetic Nanoparticles and Graphitic Carbon Nitride as the Adsorbent. *Microchimica Acta*, **185**, Article No. 18. https://doi.org/10.1007/s00604-017-2546-z

[29] Pourali, S., Amrollahi, R., Alamolhoda, S. and Masoudpanah, S.M. (2025) In Situ Synthesis of ZnO/g-C_3N_4 Based Composites for Photodegradation of Methylene Blue under Visible Light. *Scientific Reports*, **15**, Article No. 462. https://doi.org/10.1038/s41598-024-84645-0

[30] He, T., Wu, Y., Jiang, C., Chen, Z., Wang, Y., Liu, G., *et al.* (2020) Novel Magnetic

Fe_3O_4/g-C_3N_4/MoO_3 Nanocomposites with Highly Enhanced Photocatalytic Activities: Visible-Light-Driven Degradation of Tetracycline from Aqueous Environment. *PLOS ONE*, **15**, e0237389. https://doi.org/10.1371/journal.pone.0237389

[31] Jiao, Y., Zhang, H., Dong, T., Shen, P., Cai, Y., Zhang, H., *et al.* (2017) Improved Electrochemical Performance in Nanoengineered Pomegranate-Shaped Fe_3O_4/rGO Nanohybrids Anode Material. *Journal of Materials Science*, **52**, 3233-3243. https://doi.org/10.1007/s10853-016-0612-2

[32] Alves, T., Mota, W.S., Barros, C., Almeida, D., Komatsu, D., Zielinska, A., *et al.* (2024) Review of Scientific Literature and Standard Guidelines for the Characterization of Graphene-Based Materials. *Journal of Materials Science*, **59**, 14948-14980. https://doi.org/10.1007/s10853-024-10061-4

[33] Chang, X., Fan, H., Lei, L., Wu, X., Wang, W. and Ma, L. (2023) Generation Mechanism of the Defects in g-C_3N_4 Synthesized in N_2 Atmosphere and the Method for Improving Photocatalysis Activity. *Catalysts*, **13**, Article 269. https://doi.org/10.3390/catal13020269

[34] Jia, X., Dai, R., Sun, Y., Song, H. and Wu, X. (2016) One-Step Hydrothermal Synthesis of Fe_3O_4/g-C_3N_4 Nanocomposites with Improved Photocatalytic Activities. *Journal of Materials Science: Materials in Electronics*, **27**, 3791-3798. https://doi.org/10.1007/s10854-015-4224-4

[35] Isari, A.A., Payan, A., Fattahi, M., Jorfi, S. and Kakavandi, B. (2018) Photocatalytic Degradation of Rhodamine B and Real Textile Wastewater Using Fe-Doped TiO_2 Anchored on Reduced Graphene Oxide (Fe-TiO_2/rGO): Characterization and Feasibility, Mechanism and Pathway Studies. *Applied Surface Science*, **462**, 549-564. https://doi.org/10.1016/j.apsusc.2018.08.133

[36] Salehi, G., Bagherzadeh, M., Abazari, R., Hajilo, M. and Taherinia, D. (2024) Visible Light-Driven Photocatalytic Degradation of Methylene Blue Dye Using a Highly Efficient Mg-Al LDH@g-C_3N_4 @Ag_3PO_4 Nanocomposite. *ACS Omega*, **9**, 4581-4593. https://doi.org/10.1021/acsomega.3c07326

[37] Jafari, F. and Rahsepar, F.R. (2023) V_2O_5-Fe_3O_4/rGO Ternary Nanocomposite with Dual Applications as a Dye Degradation Photocatalyst and OER Electrocatalyst. *ACS Omega*, **8**, 35427-35439. https://doi.org/10.1021/acsomega.3c06094

[38] Ali, G., Jazib Abbas Zaidi, S., Abdul Basit, M. and Park, T.J. (2021) Synergetic Performance of Systematically Designed g-C_3N_4/rGO/SnO_2 Nanocomposite for Photodegradation of Rhodamine-B Dye. *Applied Surface Science*, **570**, Article 151140. https://doi.org/10.1016/j.apsusc.2021.151140

[39] Kumar, S., Kaushik, R.D. and Purohit, L.P. (2021) Hetro-Nanostructured Se-ZnO Sustained with RGO Nanosheets for Enhanced Photocatalytic Degradation of P-Chlorophenol, P-Nitrophenol and Methylene Blue. *Separation and Purification Technology*, **275**, Article 119219. https://doi.org/10.1016/j.seppur.2021.119219

[40] Roy, J.S., Dugas, G., Morency, S., Ribeiro, S.J.L. and Messaddeq, Y. (2020) Enhanced Photocatalytic Activity of Silver Vanadate Nanobelts in Concentrated Sunlight Delivered through Optical Fiber Bundle Coupled with Solar Concentrator. *SN Applied Sciences*, **2**, Article No. 185. https://doi.org/10.1007/s42452-020-1969-z

[41] Ulfa, M. and Rohmah, I.S. (2025) Thermal-induced Structural Evolution of Mesoporous Oxides Fe-Co-Ni for Enhanced Visible-Light Dye Degradation. *Next Materials*, **9**, Article 101024. https://doi.org/10.1016/j.nxmate.2025.101024

[42] Arulkumar, E., Santhosh Shree, S. and Thanikaikarasan, S. (2023) Photocatalytic Degradation Efficiency of Rhodamine-B for CuO/CdO Nanosheets Attained through

Simple Co-Precipitation Method. *Results in Chemistry*, **6**, Article 101169. https://doi.org/10.1016/j.rechem.2023.101169

[43] Chankhanittha, T., Watcharakitti, J. and Nanan, S. (2019) PVP-Assisted Synthesis of Rod-Like ZnO Photocatalyst for Photodegradation of Reactive Red (RR141) and Congo Red (CR) Azo Dyes. *Journal of Materials Science: Materials in Electronics*, **30**, 17804-17819. https://doi.org/10.1007/s10854-019-02132-z

[44] Meena, P.L., Poswal, K., Surela, A.K. and Saini, J.K. (2022) Synthesis of Graphitic Carbon Nitride/Zinc Oxide (g-C_3N_4/ZnO) Hybrid Nanostructures and Investigation of the Effect of ZnO on the Photodegradation Activity of g-C_3N_4 against the Brilliant Cresyl Blue (BCB) Dye under Visible Light Irradiation. *Advanced Composites and Hybrid Materials*, **6**, Article No. 16. https://doi.org/10.1007/s42114-022-00577-1

[45] Chiu, Y.H., Chang, T.F.M., Chen, C.Y., Sone, M. and Hsu, Y.J. (2019) Mechanistic Insights into Photodegradation of Organic Dyes Using Heterostructure Photocatalysts. *Catalysts*, **9**, Article 430. https://doi.org/10.3390/catal9050430

[46] Azeez, F., Al-Hetlani, E., Arafa, M., Abdelmonem, Y., Nazeer, A.A., Amin, M.O., *et al.* (2018) The Effect of Surface Charge on Photocatalytic Degradation of Methylene Blue Dye Using Chargeable Titania Nanoparticles. *Scientific Reports*, **8**, Article No. 7104. https://doi.org/10.1038/s41598-018-25673-5

[47] Matinise, N., Botha, N., Fall, A. and Maaza, M. (2025) Enhanced Photocatalytic Degradation of Methylene Blue Using Zinc Vanadate Nanomaterials with Structural and Electrochemical Properties. *Scientific Reports*, **15**, Article No. 26333. https://doi.org/10.1038/s41598-025-11418-8

[48] Sofia, G., Koventhan, C., Kanmani, S. and Lo, A. (2025) Green Synthesized rGO/TiO_2/g-C_3N_4 Nanocomposites via Plectranthus Amboinicus Extract for Efficient Photocatalytic Degradation of Methylene Blue: RSM Optimization, Antimicrobial and Phytotoxicity Assessment. *Journal of Environmental Chemical Engineering*, **13**, Article 115267. https://doi.org/10.1016/j.jece.2024.115267

[49] Bikerchalen, S., Akhsassi, B., Bakiz, B., Villain, S., Taoufyq, A., Guinneton, F., *et al.* (2025) Photocatalytic Degradation of Rhodamine B Dye over Oxygen-Rich Bismuth Oxychloride $Bi_{24}O_{31}Cl_{10}$ Photocatalyst under UV and Visible Light Irradiation: Pathways and Mechanism. *Journal of Physics and Chemistry of Solids*, **196**, Article 112342. https://doi.org/10.1016/j.jpcs.2024.112342

[50] Sharifian, K., Mahdikhah, V. and Sheibani, S. (2021) Ternary Ag@$SrTiO_3$@CNT Plasmonic Nanocomposites for the Efficient Photodegradation of Organic Dyes under the Visible Light Irradiation. *Ceramics International*, **47**, 22741-22752. https://doi.org/10.1016/j.ceramint.2021.04.291